Enhancing Transversal Relaxation for Magnetite Nanoparticles in MR Imaging Using Gd^{3+}-Chelated Mesoporous Silica Shells

Chih-Chia Huang,[†,∥] Chiau-Yuang Tsai,[‡,∥] Hwo-Shuenn Sheu,[§] Kuei-Yi Chuang,[†] Chiu-Hun Su,[§] U-Ser Jeng,[§] Fong-Yu Cheng,[†] Chia-Hao Su,[⊥,*] Huan-Yao Lei,[‡,*] and Chen-Sheng Yeh[†,*]

[†]Department of Chemistry and Center for Micro/Nano Science and Technology and [‡]Department of Microbiology and Immunology, National Cheng Kung University, Tainan 701, Taiwan, [§]National Synchrotron Radiation Research Center, Hsinchu 30076, Taiwan, and [⊥]Center for Translational Research in Biomedical Science, Chang Gung Memorial Hospital—Kaohsiung Medical Center, Kaohsiung 833, Taiwan. [∥]These authors contributed equally to this work.

ABSTRACT A new magnetic nanoparticle was synthesized in the form of Gd^{3+}-chelated Fe_3O_4@SiO_2. The Fe_3O_4 nanoparticle was octahedron-structured, was highly magnetic (~94 emu/g), and was the core of an encapsulating mesoporous silica shell. DOTA-NHS molecules were anchored to the interior channels of the porous silica to chelate Gd^{3+} ions. Because there were Gd^{3+} ions within the silica shell, the transverse relaxivity increased 7-fold from 97 s^{-1} mM^{-1} of Fe_3O_4 to 681 s^{-1} mM^{-1} of Gd^{3+}-chelated Fe_3O_4@SiO_2 nanoparticles with r_2/r_1 = 486. The large transversal relaxivity of the Gd^{3+}-chelated Fe_3O_4@SiO_2 nanoparticles had an effective magnetic resonance imaging effect and clearly imaged lymph nodes. Physiological studies of liver, spleen, kidney, and lung tissue in mice infused with these new nanoparticles showed no damage and no cytotoxicity in Kupffer cells, which indicated that Gd^{3+}-chelated Fe_3O_4@SiO_2 nanoparticles are biocompatible.

KEYWORDS: Fe_3O_4 · mesoporous silica · Gd chelates · relaxivity · MRI

Non-invasive magnetic resonance imaging (MRI), which does not harm the body, provides anatomical details for diagnosis and offers a highly resolved contrast between the specific tissues or organs of interest and their surrounding tissue. In the past decade, significant efforts in synthesizing nanosized particles has led to increased recognition of nanoparticles as potent MRI contrast agents because of their diverse sizes, shapes, and surface characteristics. The particle size, structure, composition, and crystallinity as well as surface chemistry all strongly affect relaxivity and contrast performance.[1−7] The chelate complexes and inorganic nanoparticles containing gadolinium (Gd) ions, with their high electron spin, contribute the observable r_1 (longitudinal relaxivity) contrast. Because of the dephasing of the water proton magnetic moments from the magnetic field gradient created by magnetized particles, magnetic nanoparticles have a greater effect on r_2 (transverse relaxivity) contrast. It is known that Fe_3O_4 (magnetite) nanoparticles are relatively friendly to the biological system, and they have been common magnetic materials in numerous biomedical applications. Unfortunately, because of their oxidized states, Fe_3O_4 nanoparticles have less saturation magnetization (M_s) than do other magnetic nanoparticles, which results in their having a limited effect on r_2 relaxivity. As a consequence, using nanomaterials with higher magnetization, such as bimetallic ferrite nanoparticles (*e.g.*, $MnFe_2O_4$ and $CoFe_2O_4$), has been an alternative.[8] Zn^{2+} dopant to increase the magnetization of Mn−Fe−O ferrite nanoparticles has also been developed.[9] However, additional transition metal ions other than iron as a contrast agent have always been a concern because of their deleterious effects on physiology.

In developing high molecular weight contrast agents, the dimeric Gd^{3+} complexes containing two paramagnetic centers in the structures, [pip{Gd(DO3A)(H_2O)}$_2$] and [bisoxa{Gd(DO3A)(H_2O)}$_2$], exhibit intermolecular and intramolecular dipole−dipole interactions between two Gd^{3+} ions, which contributes to the transverse electronic relaxation rate.[9] We have postulated that the confined geometry of a nanoscale architecture like a mesoporous structure will encapsulate Gd ions, affecting the transversal relaxation rate. In this study, we show that building a mesoporous shell over a magnetite particle surface with Gd^{3+} ions immobilized inside the confined channels significantly increased the r_2 relaxivity of Fe_3O_4 nanoparticles. In the present study, highly

* Address correspondence to csyeh@mail.ncku.edu.tw, hylei@mail.ncku.edu.tw, chiralsu@gmail.com.

Received for review January 25, 2011 and accepted April 22, 2011.

Published online April 22, 2011
10.1021/nn200306g

magnetic (94 emu/g) truncated octahedral iron oxide nanoparticles were synthesized and then subjected to sol–gel hydrolysis condensation, which yielded mesoporous silica-shelled Fe_3O_4 nanoparticles. A new type of T_2 contrast agent, Gd^{3+}-chelated Fe_3O_4@SiO_2 nanoparticles, was formed using Gd^{3+} DOTA chelate anchored inside the pore channels of the mesoporous shells. The Gd^{3+}-chelated Fe_3O_4@SiO_2 nanoparticles displayed a boost increase in transverse relaxivity. The r_2 relaxivities increased from 97 s^{-1} mM^{-1} of Fe_3O_4 to 681 s^{-1} mM^{-1} of Gd^{3+}-chelated Fe_3O_4@SiO_2 with r_2/r_1 = 486, which indicated that this is a promising candidate for a T_2 contrast agent. To our knowledge, both the r_2 and r_2/r_1 values are likely the highest values among the reported free-standing Fe_3O_4 nanocontrast agents. Usually, synthetic Fe_3O_4 nanoparticles display transversal relaxivity below 200 s^{-1} mM^{-1}. Hyeon *et al.*[10] and Cheon *et al.*[3] have reported Fe_3O_4 nanoparticles with 245 s^{-1} mM^{-1} r_2 and 72 r_2/r_1 at 1.5 T and 276 s^{-1} mM^{-1} r_2 at 4.7 T, respectively. Very recently, dendronized Fe_3O_4 nanoparticles were synthesized and exhibited a high r_2 of 349 s^{-1} mM^{-1} with a 44.8 r_2/r_1 ratio at 1.5 T.[11] As examined at 7 T, the same dendronized magnetites showed an increase of r_2/r_1 to 317 but a decreased r_2 (266 s^{-1} mM^{-1}). Copolymer-modified Fe_3O_4 nanoparticles reached an r_2 of 385 ± 39 s^{-1} mM^{-1}.[12] In addition, no published studies report creating an effective contrast agent by combining the two types with Gd ions and iron oxide nanoparticles. Either a chelating strategy with Gd ions labeled on the surface of iron oxide nanoparticles[13] or a doping method with Gd substitutions in magnetite particles[14] leads to apparently decreased relaxivities, which results in a longer transverse relaxation time (T_2). The effectiveness of Gd^{3+}-chelated Fe_3O_4@SiO_2 nanoparticles as a contrast agent was also evaluated *in vivo* for MR images of the liver, kidneys, spleen, and lymph nodes. The detection of lymph nodes shows that Gd^{3+}-chelated Fe_3O_4@SiO_2 nanoparticles are potent T_2 contrast agents in the diagnosis of metastatic lymph nodes. The physiological effects of the administered nanoparticles in mice were evaluated by observing AST and ALT levels, indicators of an injured or inflamed liver, and also by observing the status of Kupffer cells.

RESULTS AND DISCUSSION

In a typical synthesis process, magnetite nanoparticles were prepared using a thermal decomposition reaction of iron acetylacetonate, $Fe(acac)_3$, plus oleic acid and trioctylamine. Figure 1a shows a high-resolution synchrotron X-ray powder diffraction (λ = 0.49594 Å) of as-obtained iron oxide nanoparticles with the diffraction peaks of the crystalline cubic inverse spinel of bulk Fe_3O_4 (JPCDS No. 19-0629). It is known that Fe_3O_4 (magnetite) and γ-Fe_2O_3 (maghemite) have close diffraction patterns. No peaks were observed at 7.6 and 8.3°, which correspond to the reflection peaks

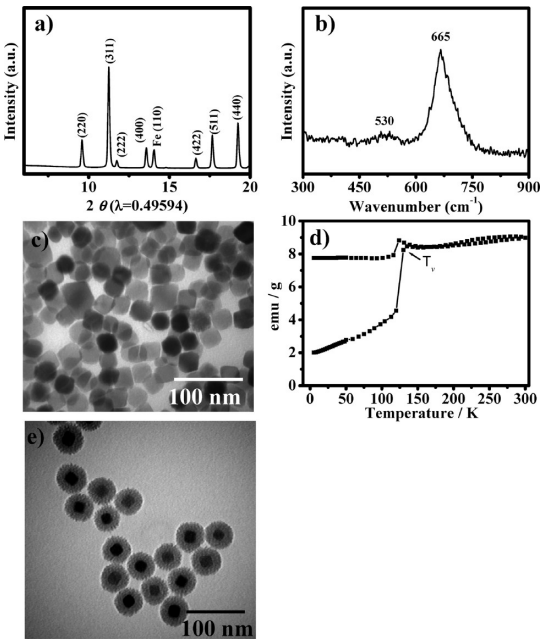

Figure 1. (a) XRD spectrum using a high-resolution synchrotron X-ray (λ = 0.49594 Å) source, (b) Raman spectrum, (c) TEM image, and (d) ZFC–FC curve for Fe_3O_4 nanoparticles. (e) TEM image for Fe_3O_4@SiO_2 nanoparticles.

(210) and (211), respectively, which are γ-Fe_2O_3 characteristic reflections that represent partial ordering of the vacancies.[15,16] The measurements of Raman-active modes have been reliable for differentiating iron oxide phases. Magnetite exhibits a strong band at approximately 670 cm^{-1}, assigned as the A_{1g} mode, accompanied with a weak transition near 540 cm^{-1} due to the T_{2g} mode. In contrast, maghemite has three characteristic bands of 720, 500, and 350 cm^{-1}, which represent the A_1, E, and T_1 modes, respectively. The particles displayed a strong band located at 665 cm^{-1} and a very weak transition centered at around 530 nm (Figure 1b). Rietveld refinement, which was used to calculate the unit cell dimension, indicated that there was no γ-Fe_2O_3 in the magnetite samples (Table S1 in Supporting Information). We were able to calculate the lattice constants using a unit cell dimension of 8.38921(8) Å.

A TEM image (Figure 1c) reveals Fe_3O_4 nanoparticles with an edge length of ~22 nm. High-resolution TEM provides structural information on Fe_3O_4 nanoparticles (Figure S1 in Supporting Information). The representative magnetites exhibited a truncated rhombohedra shape consisting of eight {111} and six {001} faces in the [110] projection. In contrast, the projected shape revealed as a truncated square was taken from the zone axis [001]. These results show that the nanoparticles had the shape of a truncated octahedron. Notably, the (110) reflection of α-Fe appeared in the magnetite. Rietveld refinement showed that the Fe_3O_4 particles contained 7.51% α-Fe (Figure 1a and Table S1). An electron diffraction pattern of a single

[001]-oriented nanoparticle provided more detailed information on the composition of Fe_3O_4 nanoparticles: it showed both magnetite and metallic Fe diffraction spots (Figure S1c). In addition, we did a fast Fourier transform (FFT) analysis on [001]-oriented 22 nm sized nanoparticles; this yielded reconstructed FFT spot patterns (Figure S1d). The reconstructed images filtered from Fe_3O_4 and Fe reflection spots showed metallic Fe embedded in magnetite nanoparticles (Figure S1e−f). Figure 1d shows the zero-field cooling (ZFC) and field cooling (FC) magnetization measurements ($M-T$ curves) at 100 Oe. A sharp feature appeared at 120 K, corresponding to the signature of the Verwey transition temperature (T_V), an indicator of chemical purity in magnetite. The Fe vacancies on the octahedral sites of magnetite have a specific function for the Verwey transition.[17,18] This, the Fe^{3+}/Fe^{2+} ratio on the octahedral sites, affects magnetic behavior and the profile of the Verwey transition. The Verwey temperature decreases as cation vacancies increase. Any modification of stoichiometry may suppress the Verwey transition. Thus, our synthesis of 22 nm sized Fe_3O_4 nanoparticles can be viewed with satisfactory stoichiometry in the formation of magnetite. It should be mentioned that the appearance of the Verwey transition remained unchanged for the resulting Fe_3O_4 nanoparticles after they had been stored in the dark for more than 4 months. The magnetization of Fe_3O_4 nanoparticles at 300 K exhibited a visible hysteresis, which suggested ferromagnetism with remanent magnetization (M_r) of 5.1 emu/g and coercivity (H_c) of 63 Oe (Figure S2 in Supporting Information). The saturation magnetization (M_s) was up to 94 emu/g (137.6 emu/$g_{[Fe]}$), which is comparable to that of bulk magnetite (92 emu/g).

The high magnetization of Fe_3O_4 nanoparticles is probably attributable to the embedded Fe. Metallic iron might have formed inside 22 nm sized magnetite because it uses unsaturated (double bond) precursors (*e.g.*, oleic acid and $Fe(acac)_3$) or because of free radical formation in our high-temperature thermo-decomposition synthesis. Compounds with double bonds act as reducing agents at high temperature,[19] which reduces Fe^{3+} to Fe^0. A reaction-time dependence analysis of Fe_3O_4 formation was done for the decomposition of $Fe^{III}(acac)_3$ at 305 °C (Figure S3 in Supporting Information). Interestingly, the FeO crystal appeared in the early reaction stage (2 min) as well as in the magnetite phase. As reaction time prolonged to 10 min, the FeO structure diminished, and the (110) reflection peak of metal Fe^0 appeared, which implied that high-temperature annealing in the inner atmosphere induced the conversion of FeO crystallites into Fe^0 and magnetite. TEM images (Figure S3a) showed that the particle size decreased to 32 nm (2 min), 28 nm (10 min), and 22 nm (30 min) as the reaction time increased, while the M_s (Figure S3b) increased from 81 emu/g for 32 nm (2 min), to 86 emu/g for 28 nm (10 min), and to 94 emu/g for 22 nm (30 min). The increase of M_s value with reaction time is likely attributable to the generation of metallic Fe. Hysteresis occurred in the 32 nm (2 min) and 28 nm (10 min) products, which indicated ferromagnetism, from the $M-H$ measurements (300 K).

The as-prepared magnetic nanoparticles were capped with oleic acids and dispersed in toluene and hexane. Oleic-acid-capped magnetite was surface-modified with CTAB surfactants so that it would solubilize in H_2O. For CTAB surfactant coating, the van der Waals interactions between the hydrophobic chains in oleic acid and CTAB led to water-soluble magnetic nanoparticles with hydrophilic charged head groups of CTAB outward giving Fe_3O_4@CTAB nanoparticles with +43.2 mV surface charges. Subsequently, the Fe_3O_4@CTAB nanoparticles were further accessed using hydrolysis condensation of the TEOS molecules forming the mesoporous silica shell around the nanoparticles. The TEOS condensation reaction was done in the basic solution with NaOH and CTAB added. CTAB micelle was the organic template that interacted with the silicate polyanion product from the base-catalyzed hydrolysis of TEOS; this allowed the assembly of silicate polyanions and CTAB surfactants to form a mesoporous silica shell on the Fe_3O_4 nanoparticle surface.[20−22] A similar strategy has been used to prepare Au rod@mesoporous silica[21] and carbon nanotube@mesoporous silica[22] nanocomposites. The Fe_3O_4@SiO_2 nanoparticles (Figure 1e) were composed of 18 nm thick silica shells with pores in the range of 2−4 nm measured from high-magnification TEM images (Figure S4). FTIR analysis characterized the Fe_3O_4@SiO_2 nanoparticles by showing silica-related vibration bands (Figure S5a). We followed a reported APTES/ethanol extraction method by adding APTES to remove the CTAB surfactants; ethanol helped to dissolve the CTAB surfactants.[23−25] FT-IR measurement indicated the disappearance of vibration peaks (3000−2800 cm^{-1}) associated with CTAB surfactants (Figure S5b). APTES molecules accessed the interior surface of the pore channels and reacted with silanol groups of mesoporous silica walls. The APTES-treated Fe_3O_4@SiO_2 nanoparticles were then conjugated with DOTA-NHS molecules *via* amide bonds. It should be noted that FT-IR analysis also indicated that DOTA had attached to the surface of APTES-treated Fe_3O_4@SiO_2 nanoparticles, as well (Figure S5c). The small shoulder at ∼1730 cm^{-1} (carboxylic acid group) and signals at 1530−1340 cm^{-1} (ionized carboxyl group) originated from DOTA. The same surface modification strategy allowed us to prepare DOTA-functionalized silica nanotubes in our previous work.[26] The DOTA molecules render high affinity to chelated Gd^{3+} ions inside the mesoporous silica channels, yielding Gd^{3+}-chelated Fe_3O_4@SiO_2 nanoparticles. The amine-functionalized silanes acted as a linker to form amide bonds with the Gd-chelated

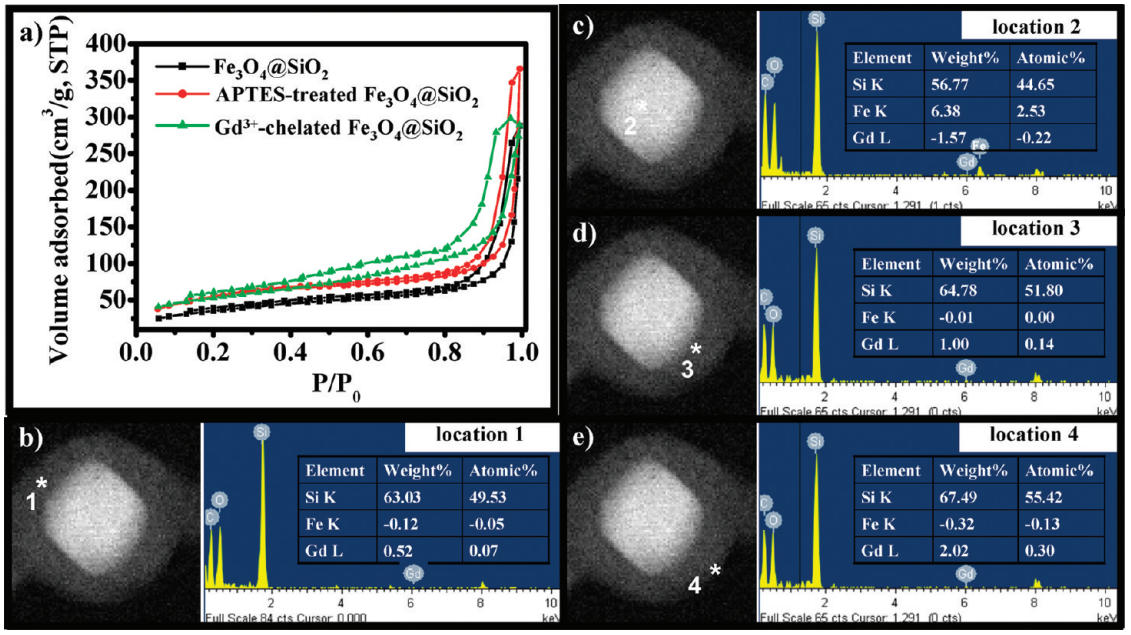

Figure 2. (a) BET analysis for Fe_3O_4@SiO_2, APTES-treated Fe_3O_4@SiO_2, and Gd^{3+}-chelated Fe_3O_4@SiO_2 nanoparticles. (b−e) HAADF STEM (high angle annular dark field scanning transmission electron microscopy) image of a single Gd^{3+}-chelated Fe_3O_4@SiO_2 nanoparticle. EDS analysis in the spot-capture mode was performed in four different positions (marked as ∗ and labeled 1−4) of the particle using an electron beam 2 nm in diameter.

complex on one side, while the siloxane linked with the interior surface of the silica on the other side. Although Gd^{3+} chelating on the outmost surface of mesoporous SiO_2 nanoshells cannot be excluded because of the DOTA conjugated on the surface, previous studies[27−29] have succeeded in grafting Gd chelates inside mesoporous pores. Further performance in small-angle X-ray scattering (SAXS) measurements discussed later provides the evidence of Gd^{3+} ions immobilized inside the pores. High-magnification TEM images of Gd^{3+}-chelated Fe_3O_4@SiO_2 nanoparticles (Figure S6) show the same morphology as those of Fe_3O_4@SiO_2 nanoparticles. The Gd^{3+}-chelated Fe_3O_4@SiO_2 nanoparticles have a positive surface charge of +17.4 mV. XPS analysis (Figure S7) shows a broad band in the range of 135−140 eV corresponding to Gd_{4d},[30] which indicates the presence of Gd^{3+} ions in DOTA-functionalized Fe_3O_4@SiO_2 compared with Fe_3O_4@SiO_2 nanoparticles. No detection of an Fe signal is consistent with core−shell nanostructures. The Si 2p appeared at around 103−105 eV for both Gd^{3+}-chelated Fe_3O_4@SiO_2 and Fe_3O_4@SiO_2 samples.

The specific surface area (BET plot) of Fe_3O_4@SiO_2 nanoparticles treated with APTES was larger at 200 m^2/g than that of the Fe_3O_4@SiO_2 nanoparticles not treated with APTES (130 m^2/g) (Figure 2a). However, the surface area of Gd^{3+}-chelated Fe_3O_4@SiO_2 nanocomposites was reduced to 186 m^2/g after the incorporation of Gd^{3+}. BJH analysis (Figure S8) shows pore size distributions for Fe_3O_4@SiO_2, APTES-treated Fe_3O_4@SiO_2, and Gd^{3+}-chelated Fe_3O_4@SiO_2 nanoparticles. Fe_3O_4@SiO_2 with an average pore volume of 0.44 cm^3/g exhibits disorder and inhomogeneous pore sizes in the range of 2 to 8 nm. When the Fe_3O_4@SiO_2 nanoparticles were treated with APTES to remove CTAB surfactants, the small pore size contribution (<3 nm) increased, and the pore volume expanded to 0.53 cm^3/g. The overall pore volume was lower (0.46 cm^3/g) in Gd^{3+}-chelated Fe_3O_4@SiO_2 nanoparticles. HAADF STEM images combined with EDS analysis in the spot-capture mode in four different positions of a single particle were used to characterize Fe and Gd compositions (Figure 2b−e). This clearly indicated that an Fe signal appeared in the core (location 2) and that Gd was included in the silica shell (locations 1, 3, and 4). The average molar ratio of Gd/Fe was ∼0.03, which corresponds to 7.8 wt % Gd in Fe + Gd, with ∼4875 Gd^{3+} ions in a single Fe_3O_4@SiO_2 nanoparticle based on ICP-AES measurements. The magnetization of Fe_3O_4@SiO_2, and Gd^{3+}-chelated Fe_3O_4@SiO_2 nanoparticles at 300 K exhibited visible hysteresis, which suggested ferromagnetism: M_r = 26.6 emu/$g_{[Fe]}$ and H_c = 87.3 Oe for Fe_3O_4@SiO_2, and M_r = 18.2 emu/$g_{[Fe]}$ and H_c = 68.2 Oe for Gd^{3+}-chelated Fe_3O_4@SiO_2 (Figure S9). The saturation magnetizations (M_s) of Fe_3O_4@SiO_2 and Gd^{3+}-chelated Fe_3O_4@SiO_2 nanoparticles were 129 emu/$g_{[Fe]}$ (54 emu/g) and 122 emu/$g_{[Fe]}$ (51 emu/g), respectively. Leaching experiments were done to study the stability of Gd^{3+}-chelated Fe_3O_4@SiO_2 nanoparticles. A small amount (∼1.8%) of the Gd^{3+} ions was leached from nanoparticles (∼4875 of Gd^{3+} ions per Fe_3O_4@SiO_2 nanoparticle) in phosphate buffered saline solution after they had been incubated for 7 days. After they had been stored for 4 months, Gd^{3+}-chelated

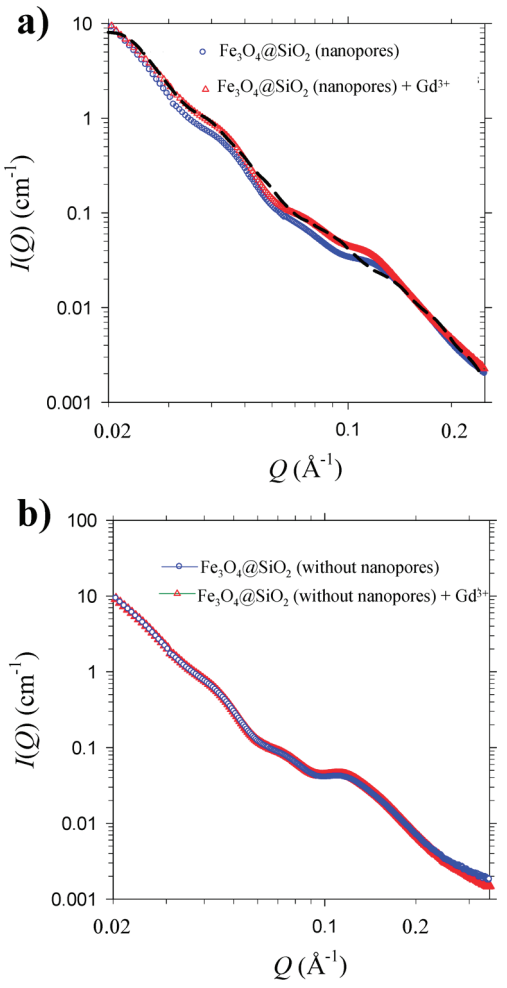

Figure 3. (a) SAXS data for the Fe_3O_4@SiO_2 nanoparticles with nanopores and that, with Gd^{3+} ions, filled in the nanopores of the SiO_2 shell. Data for Gd^{3+}-chelated Fe_3O_4@SiO_2 nanoparticles are fitted with a model of polydispersed core−shell spheres (dashed curve) of large sizes and small ellipsoid-like nanopores. (b) Overlapped SAXS profiles for the Fe_3O_4@SiO_2 nanoparticles without nanopores in a pure water solution and in a similar solution but with Gd^{3+} ions.

Fe_3O_4@SiO_2 nanoparticles remained well-dispersed in water and exhibited no change of morphology or particle size.

Figure 3a shows the small-angle X-ray scattering (SAXS) data measured for the water solutions containing Fe_3O_4@SiO_2 nanoparticles (after APTES treatment) and shows that the Gd^{3+}-chelated Fe_3O_4@SiO_2 nanoparticles infiltrated the pores of the SiO_2 shell. With a 15 keV (wavelength λ = 0.827 Å) beam and a sample-to-detector distance of 1820 cm, SAXS data analysis was done at the BL23A SWAXS end station of the National Synchrotron Radiation Research Center, Taiwan.[31] With Gd^{3+} ions adsorbed into the pores of the SiO_2 shell, giving it increased electron density, the Gd^{3+}-chelated Fe_3O_4@SiO_2 nanoparticles exhibit a stronger scattering, especially in the lower Q region (<0.1 $Å^{-1}$) dominated by the global core−shell structure. Here, the scattered wave vector Q is defined by $4\pi\lambda^{-1}\sin\theta$ (with 2θ as the scattering angle). In the higher Q region, >0.12 $Å^{-1}$, the scattering is dominated by small nanopores or is filled with Gd^{3+} ions. A model of polydispersed core−shell spheres for the large Fe_3O_4@SiO_2 nanoparticles, together with an ellipsoid model for small nanopores in the SiO_2 shell,[32] fits the data well (Figure 3a). The fitted parameters include the Fe_3O_4 core diameter of 21 ± 1 nm and the SiO_2 shell thickness of 13.6 ± 1 nm, together with a common polydispersity of 40% in core and shell sizes. The nanopores (which were filled with Gd^{3+} ions) were fitted using an approximate shape of oblate ellipsoids of 2 and 5 nm in the major and minor axis directions of the ellipsoids. The structural parameters obtained from the SAXS analysis are consistent with those observed using the corresponding TEM images and BJH analysis. For comparison, without nanopores in the SiO_2 shell, well-overlapped SAXS profiles for the Fe_3O_4@SiO_2 nanoparticles (CTAB surfactants had not been removed: "without nanpores") in a pure water solution and a similar solution with Gd^{3+} ions (Figure 3b) indicate no Gd^{3+} adsorption to the nanoparticles with no nanopores because there was CTAB inside the pores preventing the Gd^{3+} from entering. "Fe_3O_4@SiO_2 (without nanopores) + Gd^{3+}" indicates that Fe_3O_4@SiO_2 nanoparticles with CTAB surfactants were physically mixed with Gd^{3+} ions using $GdCl_3$.

To access the relaxation rate and MR imaging contrast effect, Fe_3O_4@CTAB, APTES-treated Fe_3O_4@SiO_2, Gd^{3+}-chelated Fe_3O_4@SiO_2, and commercial Resovist nanocontrast agents using different Fe ion concentrations in 0.5% agarose gel were evaluated in a 3T MRI system.[1] The T_2-weighted images substantially darkened as the concentrations of Fe ions increased for all iron oxide agents. The transverse relaxation rates ($1/T_2$) were evaluated, giving r_2 relaxivity coefficients of 97 s^{-1} mM^{-1} (Fe_3O_4@CTAB), 211.8 s^{-1} mM^{-1} (APTES-treated Fe_3O_4@SiO_2), 681 s^{-1} mM^{-1} (Gd^{3+}-chelated Fe_3O_4@SiO_2), and 91 s^{-1} mM^{-1} (Resovist). Interestingly, the r_2 value increased 7-fold from Fe_3O_4@CTAB to Gd^{3+}-chelated Fe_3O_4@SiO_2. In contrast, the r_1 relaxivity was not apparently affected, giving ~0.9 and ~1.4 s^{-1} mM^{-1} for Fe_3O_4@CTAB and Gd^{3+}-chelated Fe_3O_4@SiO_2, respectively (Figure S10). Although the detailed mechanisms involved in the increased transverse relaxivity are not clear at this stage, we hypothesize that the boost in transversal relaxivity is attributable to the contribution of geometrical confinement effect, dipolar interaction between neighboring Gd^{3+}−Gd^{3+} ions, and Curie spin relaxation. As evidenced in the case of APTES-treated Fe_3O_4@SiO_2, the r_2 values increased from 97 (Fe_3O_4@CTAB) to 211.8 s^{-1} mM^{-1} after the deposition of the mesoporous silica shell on the surface of Fe_3O_4. The confined characteristics of the mesoporous shell could have had an important effect on the relaxation rate. The large surface area of the porous shell confined the water

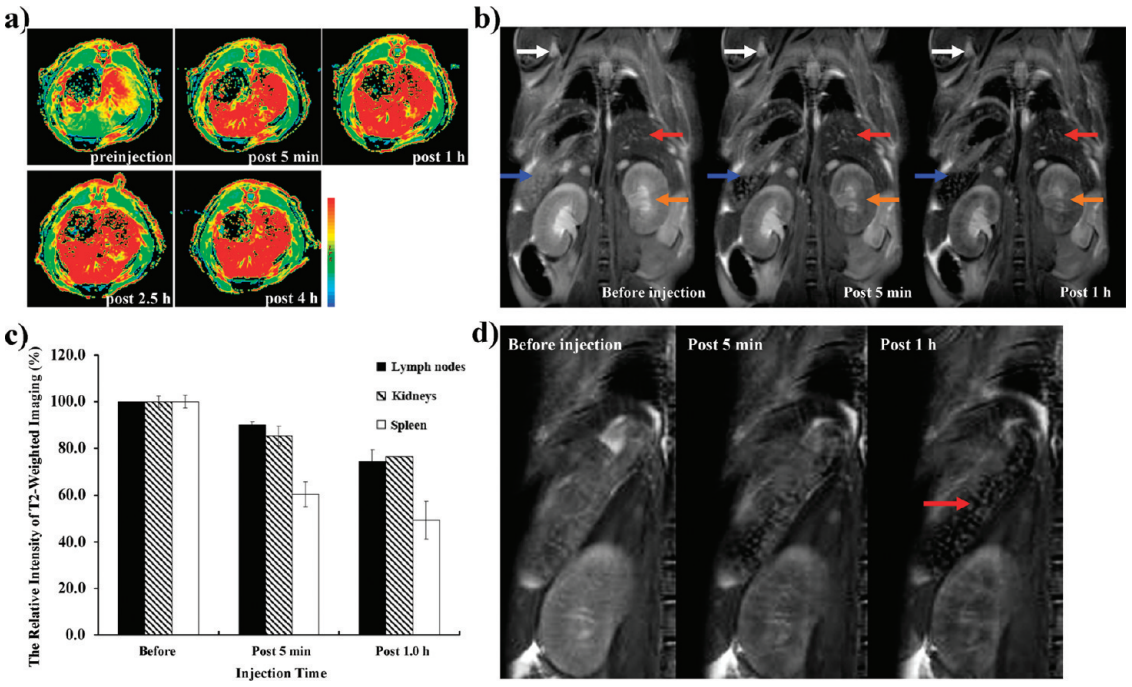

Figure 4. Gd^{3+}-chelated Fe_3O_4@SiO_2 nanoparticles with which rats and mice had been treated (dose: 0.5 mg [Fe]/kg). (a) Color R_2* mapping of a rat liver at five time points (preinjection, 5 min, 1 h, 2.5 h, and 4 h postinjection) using a clinical 3T scanner. (b) *In vivo* micro-T_2-weighted imaging of mice at three time points (preinjection, 5 min, and 1 h postinjection) (white arrows, lymph node; red arrows, liver; blue arrows, spleen; and orange arrows, kidneys) using a 7T animal micro-MRI system. (c) Signal intensities in lymph nodes, kidneys, and spleen at the three time points. (d) Progressive micro-T_2-weighted images of the spleen. The red arrow indicates the follicles of the spleen.

molecules inside the interior channels. The confined space limited the exchange rate between water inside the silica channels and the bulk water. It has been demonstrated that the formation of a second coordination shell, involving hydrogen bonding between water and polar groups of Gd^{3+} chelates, provided an outer sphere contribution that caused a strong increase in relaxivity.[33] Like the Gd^{3+} complexes, the trapped water inside the silica pores may result in reduced mobility of the hydration layer that contributes relaxivity. The additional mechanism might involve the dipolar interaction between Gd^{3+} ions with the facilitation-of-confinement characteristic. In the development of high molecular weight contrast agents, dimeric Gd^{3+} complexes containing two paramagnetic centers in the structures, [pip{Gd(DO3A)(H_2O)}$_2$] and [bisoxa{Gd(DO3A)(H_2O)}$_2$], have been observed to exhibit intermolecular and intramolecular dipole–dipole interactions between two Gd^{3+} ions that contribute to the transverse electronic relaxation rate.[9] The r_2 relaxivity of the Gd^{3+}-chelated Fe_3O_4@SiO_2 nanoparticles increased to three times that of Fe_3O_4@SiO_2. We estimated that there were ~4875 Gd^{3+} ions in the mesoporous shell of a single Fe_3O_4 nanoparticle. A considerable number of Gd^{3+} ions were immobilized in the interior of the pore channels. It is possible that the dipole–dipole coupling of the neighboring Gd^{3+}–Gd^{3+} ions interacting with each other generated increased transverse electronic relaxation. Reducing the amount of chelated Gd^{3+} in Gd^{3+}-chelated Fe_3O_4@SiO_2 nanoparticles induced a decrease in r_2 values of 384 s^{-1} mM^{-1} (Gd/Fe ~0.02) and 275 s^{-1} mM^{-1} (Gd/Fe ~0.01) (Figure S11 in Supporting Information). Last, but not least, preliminary examinations of T_1 and T_2 as a function of magnetic field displayed typical Curie relaxation behavior for Gd^{3+}-chelated Fe_3O_4@SiO_2 nanoparticles (Gd/Fe ~0.03). T_2 relaxation time is sensitive to magnetic field, showing faster relaxation at higher fields (48.6 ms at 300 MHz, 33.4 ms at 400 MHz, and 19.2 ms at 500 MHz NMR), while T_1 is substantially independent (1.8 s at 300 MHz, 2.4 s at 400 MHz, and 2.6 s at 500 MHz NMR). For large molecules at a high field, the magnetic dipolar interaction between water nuclear spin and the thermally averaged electronic spin (Curie spin) associated with paramagnetic species is strongly affected by molecular rotation dominating transversal relaxation.[34]

The large T_2 shortening effect reported here afforded faster and better T_2-weighted contrast enhancement for MRI applications. We began by examining the MRI effect *in vivo* and compared it with the MRI effect when using commercial Resovist agent. Rats were treated with nanoparticles (0.5 mg/kg), and blood-oxygen-level dependence (BOLD) MR images were acquired at different times using a clinical 3T scanner. The BOLD technique is based on the difference in contrast-agent-induced susceptibility—including the magnetic susceptibility difference between blood

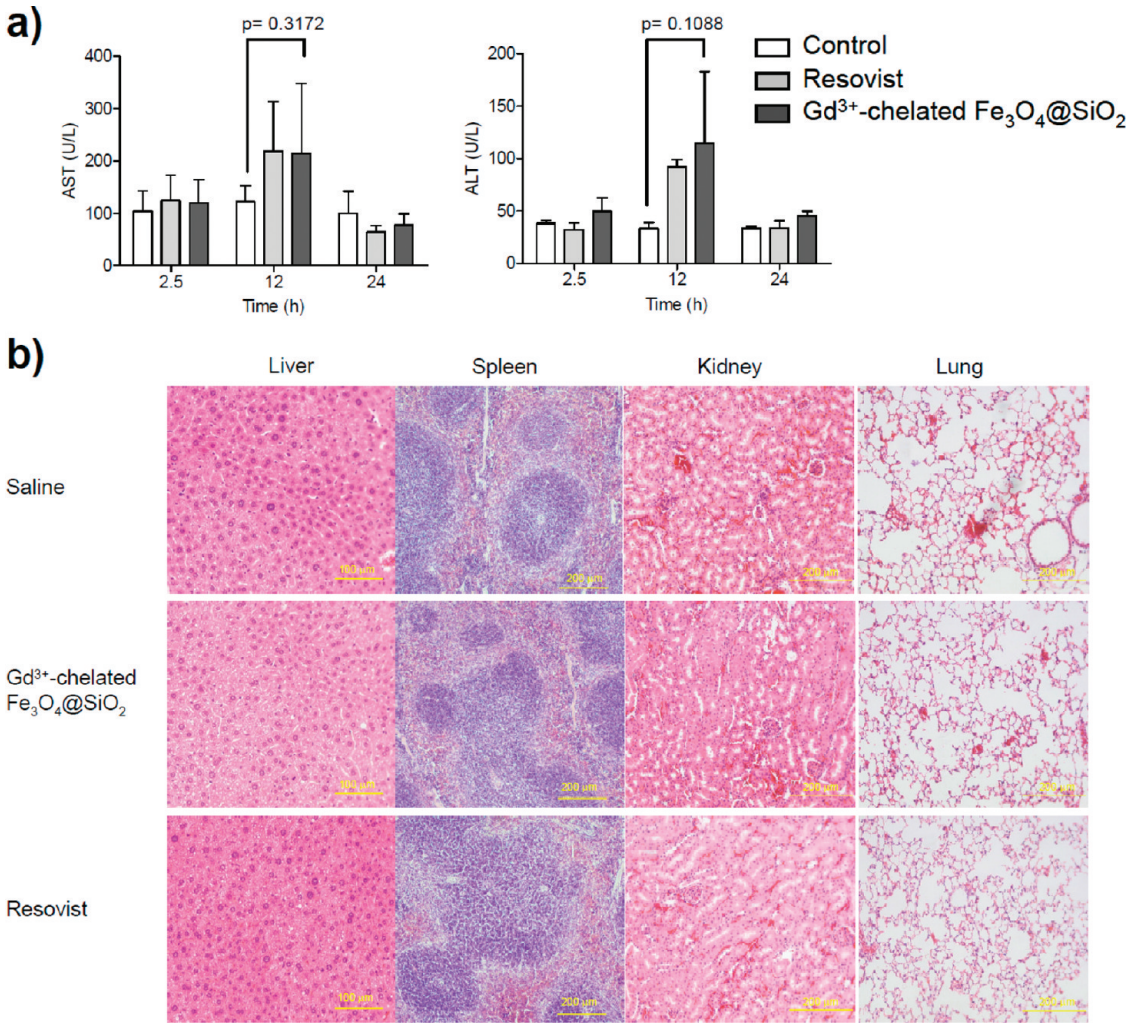

Figure 5. Evaluation of the cytotoxicity of Gd^{3+}-chelated Fe_3O_4@SiO_2 nanoparticles *in vivo*. (a) Mice were intravenously injected with 0.5 mg [Fe]/kg of Gd^{3+}-chelated Fe_3O_4@SiO_2 nanoparticles and Resovist, respectively. The serum AST and ALT levels were determined at 2.5, 12, and 24 h postinjection. Saline was used as a control. Error bars represent standard deviations from triplicate samples. (b) Histological analysis of liver, spleen, kidney, and lung tissue from Gd^{3+}-chelated Fe_3O_4@SiO_2 nanoparticles and compared with saline-treated and Resovist-treated mice. Mice were intravenously injected with respective 5 mg [Fe]/kg of Gd^{3+}-chelated Fe_3O_4@SiO_2 nanoparticles or Resovist for 24 h. Tissue samples were stained with hematoxylin and eosin.

vessels and surrounding tissue—between the pre- and postcontrast images. We introduced the BOLD sequence to acquire T_2* signals at different TEs and calculated ΔR_2 and ΔR_2* mapping at the same time. The ΔR_2 and ΔR_2* mapping reflected the degree of contrast enhancement and the change of blood volume in the vessels.[35,36] We evaluated the contrast efficiencies of Gd^{3+}-chelated Fe_3O_4@SiO_2 nanoparticles and Resovist agent. Figure 4a shows the color R_2* maps generated by the Gd^{3+}-chelated Fe_3O_4@SiO_2 nanoparticles; the regions of interest (ROIs) were placed in the liver parenchyma (outside of the vascular structure of the liver graft). The imaging contrast was immediately affected and darkened after 5 min. The signal in the liver quickly decreased to ~50% after 5 min, and then decayed to ~40% after 1 h for Gd^{3+}-chelated Fe_3O_4@SiO_2 nanoparticles. Resovsit agent showed a slow signal drop of ~60% after 4 h (Figure S12). Gd^{3+}-chelated Fe_3O_4@SiO_2 nanoparticles display better contrast enhancement than Resovist at same injection time.

We further tested Gd^{3+}-chelated Fe_3O_4@SiO_2 nanoparticles using a higher field with a 7T animal micro-MRI system. The contrast signal of the lymph nodes (white arrows), liver (red arrows), spleen (blue arrows), and kidneys (orange arrows) were all reduced after Gd^{3+}-chelated Fe_3O_4@SiO_2 administration (Figure 4b). The intensity of the lymph node, kidneys, and spleen dropped to 74, 76, and 49% after 1 h, respectively, in T_2-weighted images (Figure 4c). The spleen is rich in macrophage cells that uptake more nanoparticles, which leads to a larger reduction in contrast. Detecting lymph node metastasis is important during diagnosis, tumor staging, and subsequent clinical treatment.

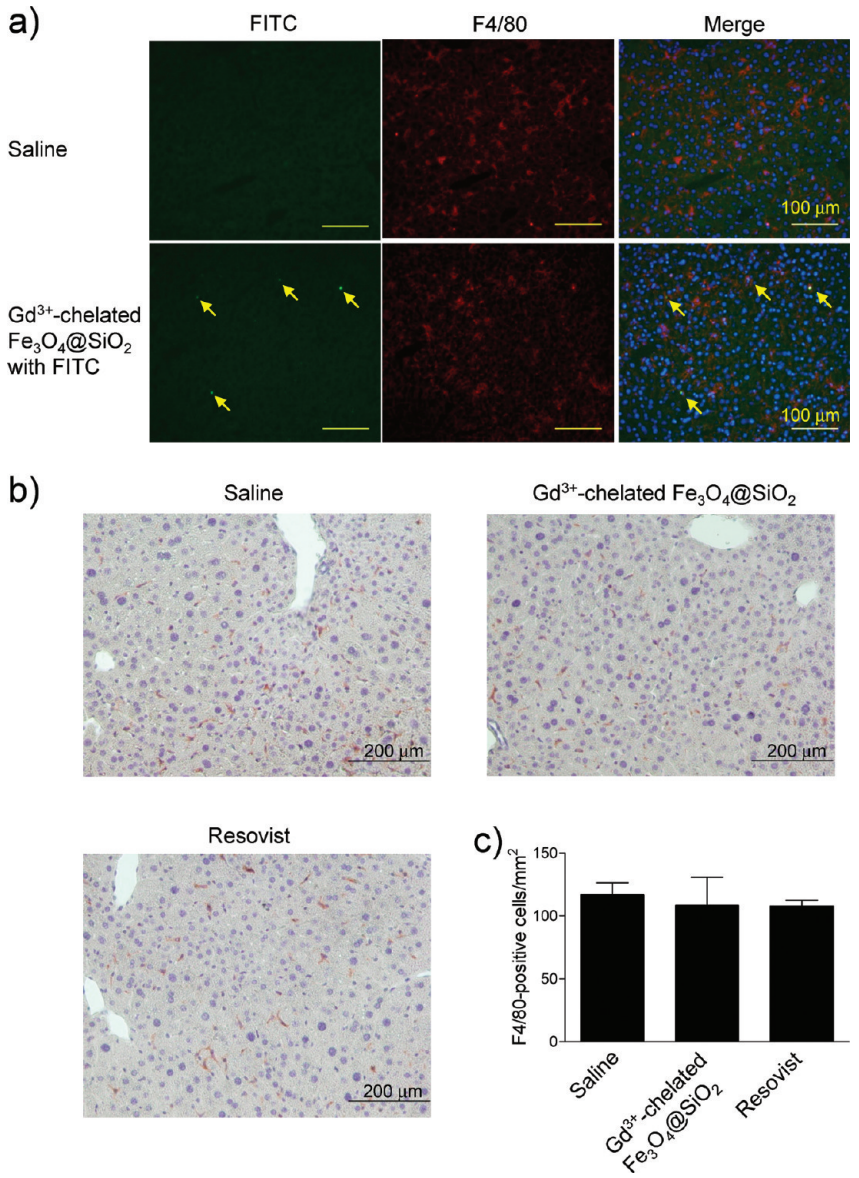

Figure 6. Gd^{3+}-chelated Fe_3O_4@SiO_2 nanoparticles were uptaken by F4/80$^+$ Kupffer cells without causing any cell death. (a) FITC nanoparticles containing Gd^{3+}-chelated Fe_3O_4@SiO_2 were colocalized with F4/80$^+$ Kupffer cells. Thirty minutes before the analysis, mice had been intravenously injected with 0.5 mg [Fe]/kg of Gd^{3+}-chelated Fe_3O_4@SiO_2 containing FITC nanoparticles or Resovist, respectively. The frozen live tissue sections were stained with anti-F4/80 antibody and then anti-rat Alexa 594 (red). The nucleus was stained with Hoechst 33258 (blue). The arrows indicate the colocalized sites. (b) Gd^{3+}-chelated Fe_3O_4@SiO_2 nanoparticles did not eliminate F4/80$^+$ Kupffer cells. Twenty-four hours before the histological analysis, mice had been intravenously injected with 5 mg [Fe]/kg of Gd^{3+}-chelated Fe_3O_4@SiO_2 nanoparticles or Resovist, respectively. The deparaffinized liver tissue sections were stained with anti-F4/80 antibody. F4/80$^+$ Kupffer cells are stained red. The nuclei were stained with hematoxylin (blue). (c) Number of F4/80$^+$ Kupffer cells after treatment with saline, Resovist, and Gd^{3+}-chelated Fe_3O_4@SiO_2 nanoparticles.

Iron oxide nanoparticles accumulate only in the normal nodes in the presence of macrophages. Gd^{3+}-chelated Fe_3O_4@SiO_2 nanoparticle images showed that the lymph node had a long-axis diameter of 2.6 mm and a short-axis diameter of 1.3 mm, which suggested that it was potent for detecting metastatic lymph nodes using Fe_3O_4/Gd nanocomposites. Furthermore, the microstructure of the spleen was clearly visualized and showed follicles (white spots) distributed in the spleen (Figure 4d). The size of the follicles was estimated to be 0.6 mm. The quantitative biodistribution (liver, lungs, kidneys, spleen, and blood) was measured in mice intravenously injected with Gd^{3+}-chelated Fe_3O_4@SiO_2 and Resovist agent following intravenous administration at different time points (Figure S13). Both types of iron oxide nanoparticles accumulated primarily in the liver. Gd^{3+}-chelated Fe_3O_4@SiO_2 reached a peak after 2.5 h and then decreased after 12 h. The Resovist agent exhibited a gradual decrease over time. Because we used a substantially smaller amount of Gd^{3+} ions than iron component, the distribution of Gd^{3+} ions was observed only in liver due to the detection

limits of the ICP-AES instrument. Iron staining showed that Gd^{3+}-chelated $Fe_3O_4@SiO_2$ nanoparticles were well-distributed in the liver (Figure S14).

A characterization of physiological effects is required for the continued development of Gd^{3+}-chelated $Fe_3O_4@SiO_2$ nanoparticles. When the liver is injured or inflamed, the levels of AST and ALT and pro-inflammatory cytokines, including tumor necrosis factor (TNF)-α and interleukin (IL)-6 in the blood, usually rise. For Gd^{3+}-chelated $Fe_3O_4@SiO_2$-treated and Resovist-treated mice with 0.5 mg [Fe]/kg per injection dose, we found that AST and ALT levels were slightly increased 12 h postinjection and returned to normal at 24 h postinjection (Figure 5a). The differences in serum AST and ALT levels between Gd^{3+}-chelated $Fe_3O_4@SiO_2$-treated mice and control mice were not significant. We did not detect any TNF-α or IL-6 levels at 0.5 or 2.5 h postinjection. When we increased the dose of Gd^{3+}-chelated $Fe_3O_4@SiO_2$ nanoparticles to 5 mg [Fe]/kg, the histological analysis of the liver, spleen, kidney, and lung tissue also showed no change in the cellular structures at 24 h postinjection (Figure 5b). This indicated that Gd^{3+}-chelated $Fe_3O_4@SiO_2$ nanoparticles did not cause any apparent tissue injury or inflammation. Although AST and ALT levels in the serum of Gd^{3+}-chelated $Fe_3O_4@SiO_2$ nanoparticle-treated mice were slightly higher at 12 h postinjection, we saw no liver damage at 24 h postinjection, even when the dose had been increased to 5 mg [Fe]/kg. The transient increase in AST and ALT levels in serum appears to be a common response of the body because other magnetite nanoparticles also induced a similar response,[37] including the Resovist used in our study.

To investigate Gd^{3+}-chelated $Fe_3O_4@SiO_2$ nanoparticles engulfed in liver cells, we gave mice intravenous fluorescein isothiocyanate (FITC)-anchored Gd^{3+}-chelated $Fe_3O_4@SiO_2$ nanoparticles (0.5 mg [Fe]/kg). The FITC dye molecules were encapsulated in the porous shells of Gd^{3+}-chelated $Fe_3O_4@SiO_2$ nanoparticles to facilitate observation of their localization in liver tissue. Figure 6a indicates that Gd^{3+}-chelated $Fe_3O_4@SiO_2$-containing FITC nanoparticles were colocalized with F4/80$^+$ Kupffer cells at 0.5 h postinjection. $GdCl_3$ not only blocks phagocytosis by Kupffer cells but also eliminates Kupffer cells.[38] Although we found little leakage (~1.8%) of Gd^{3+} ions after 7 days of *in vitro* incubation, the cytotoxicity of Gd^{3+}-chelated $Fe_3O_4@SiO_2$ nanoparticles for Kupffer cells remains a concern. After the dose had been increased to 5 mg [Fe]/kg, Gd^{3+}-chelated $Fe_3O_4@SiO_2$ nanoparticles did not cause the cell death of Kupffer cells at 24 h postinjection (Figure 6b). The estimation of the number of F4/80$^+$ Kupffer cells was not lower after they had been treated with Gd^{3+}-chelated $Fe_3O_4@SiO_2$ nanoparticles (Figure 6c). Our results suggest that Gd^{3+}-chelated $Fe_3O_4@SiO_2$ nanoparticles did not induce cytotoxicity in Kupffer cells.

CONCLUSION

We synthesized a new type of magnetic nanoparticle composed of Fe_3O_4 plus Gd^{3+}: a Gd^{3+}-chelated $Fe_3O_4@SiO_2$ nanoparticle. The immobilization of Gd^{3+} ions inside the interior channels of a mesoporous silica shell enhanced the transverse relaxation rate, which led to a large r_2 relaxivity. For short-term cytotoxicity studies, this new T_2 contrast agent showed no adverse effect on organ tissues or Kupffer cells. With this designation strategy, we expect that additional promising T_2 contrast agents using higher magnetization of the magnetic nanoparticles will be created.

MATERIALS AND METHODS

Materials. Aminopropyltriethoxysilane (APTES, 99%) (Acros, Thermo Fisher Scientific, Geel, Belgium), tetraethyl orthosilicate (TEOS, 98%) (Acros), DOTA-NHS ester (Macrocyclics, Dallas, TX), ethanol (99.9%) (J.T. Backer, Inc., Phillipsburg, NJ), L-ascorbic acid (99.7%) (Honeywell Riedel-de Haën, Hanover, Germany), $GdCl_3 \cdot 6H_2O$ (99.5%) (Sigma-Aldrich Co., St Louis, MO), iron(III) acetylacetonate (97%) (Sigma-Aldrich), oleic acid (90%) (Sigma-Aldrich), trioctylamine (98%) (Sigma-Aldrich), and cetyltrimethylammonium bromide (CTAB, 99+%) (Acros) were purchased and used without further purification.

Synthesizing Fe_3O_4 Nanoparticles. In a typical synthesis process, magnetite nanoparticles were prepared using a thermal decomposition reaction of iron acetylacetonate, $Fe(acac)_3$, in the presence of oleic acid and trioctylamine.[39] The 22 nm sized Fe_3O_4 nanoparticles were synthesized using 1.42 g of $Fe(acac)_3$ and 0.57 mL of oleic acid. The mixture solution was then refluxed at 305 °C in an Ar environment. After they had been cooled to room temperature, the precipitates were collected and washed using a toluene/ethanol (v/v = 1:4) solution.

Surface Modifications of Magnetite Nanoparticles with CTAB. To improve the hydrophilic nature of magnetite nanoparticles, a typical procedure was followed: the as-synthesized nanoparticles (22 nm, ~2.5 mg) were centrifuged and transferred to chloroform solutions. The chloroform solutions (0.5 mL) were then redispersed in 4 mL CTAB solutions (0.1 M) and sonicated for more than 2 h until the chloroform evaporated, leaving black aqueous solutions. The resulting magnetite nanoparticles were collected using centrifugation and then washed three times with distilled water.

Synthesizing Gd^{3+}-Chelated $Fe_3O_4@SiO_2$ Nanoparticles. The mesoporous silica-coated Fe_3O_4 ($Fe_3O_4@SiO_2$) nanoparticles were synthesized as follows: 0.25 mL of Fe_3O_4@CTAB solution was dispersed in 4.2 mL of CTAB (5.4 mM) and NaOH solution (1.4 mM). Next, 0.024 mL of TEOS was added dropwise into the mixture solution and stirred vigorously at 55 °C in a water bath for 4 h. While the $Fe_3O_4@SiO_2$ nanoparticles were being prepared, some aggregates yielding black precipitates were observed. To completely remove these aggregates, the as-prepared $Fe_3O_4@SiO_2$ colloidal solutions (black color) were centrifuged at 3500 rpm for 5 min, and the supernatants were collected for further preparation. Subsequently, APTES/ethanol extraction was used to remove the CTAB from the mesoporous silica shells of $Fe_3O_4@SiO_2$ nanoparticles.[23−25] The 5 mg of $Fe_3O_4@SiO_2$ nanoparticles was then suspended in ethanol at 80 °C using a reflux process. APTES (0.04 mL) was added to yield APTES-treated $Fe_3O_4@SiO_2$ nanoparticles. The APTES-treated $Fe_3O_4@SiO_2$ colloidal solutions were centrifuged at 15 000 rpm

for 15 min to remove excess CTAB surfactants. The collected precipitates (APTES-treated Fe_3O_4@SiO_2 nanoparticles) were washed in ethanol. This centrifugation–washing procedure was repeated three times. Next, the DOTA-NHS chelate agents were used to form amide bonds with APTES molecules. In a typical preparation, 3 mg of APTES-modified Fe_3O_4@SiO_2 nanoparticles was suspended in 3 mL of DOTA-NHS (12 mM) aqueous solution overnight. The resulting products were collected using centrifugation and then washed three times with distilled water to remove excess DOTA-NHS. The DOTA-conjugated Fe_3O_4@SiO_2 nanoparticles (3 mg) were resuspended in 3 mL of 12 mM $GdCl_3$ for 12 h to yield Gd^{3+}-chelated Fe_3O_4@SiO_2 nanoparticles. The excess Gd^{3+} ions were removed using centrifugation at 14 000 rpm for 15 min, and then the collected Gd^{3+}-chelated Fe_3O_4@SiO_2 nanoparticles were washed in H_2O. This centrifugation–washing procedure was repeated three times. ICP analysis was used to determine that there were no Gd^{3+} ions in the supernatants after the third centrifugation. Gd^{3+}-chelated Fe_3O_4@SiO_2 nanoparticles were incubated with the L-ascorbic acid (1 mM) for 1 day before additional *in vitro* and *in vivo* analyses.

***In Vitro* Magnetic Resonance Imaging (MRI) Assays.** The experiments in this study were done using a spectroscope (3T MRI Biospec; Bruker Optik GmbH, Ettlingen, Germany).[1,2] A gradient system mounted on the table of a 3T magnet (inner diameter = 6 cm; maximal gradient strength = 1000 mT m^{-1}) was used to yield high-resolution images. A quadrature coil (inner diameter = 3.5 cm) was used for RF transmission and reception. For T_2 measurement, the Fe_3O_4@CTAB, Fe_3O_4@SiO_2, and Gd^{3+}-chelated Fe_3O_4@SiO_2 nanoparticles and the commercial Resovist agent with various concentrations of iron were dispersed in a 0.5% agarose gel solution. The acquired MRIs (matrix size = 256 × 192; field of view = 60 × 60 mm^2; slice thickness = 3 mm) had an in-plane resolution of 234 μm after image smoothing. T_1 values were measured using a multislice multiecho sequence with a T_R of 6000 ms, a T_E of 8.7 ms, and 45 inversion recovery points (T_I = 13.3–6000 ms; field of view = 60 × 60 mm^2; slice thickness = 6 mm; image matrix = 128 × 128). This allowed for simultaneous imaging of 26 vials with 0.3 mL of contrast agent per vial. An average signal of 50 voxels was evaluated for all T_I values. T_2 values were measured with a spin–echo sequence of T_R/T_E of 4000/10.1 ms, 60 echo points with 60 different echo times, and a NEX of 5 (field of view = 60 × 60 mm^2; slice thickness = 6 mm; imaging plane = 256 × 192). The resulting r_1 and r_2 values were measured based on the inverse relaxation time ($1/T_2$) *versus* iron ion concentrations in 0.5% agarose gel.

***In Vivo* Blood-Oxygen-Level Dependence (BOLD) MR Imaging.** Male Sprague–Dawley rats (6–8 weeks old) were provided by the Chang Gung Memorial Hospital–Kaohsiung Medical Center Laboratory Animal Center (Tainan, Taiwan). The rats were given humane care that complied with the Chang Gung Memorial Hospital–Kaohsiung Medical Center's Animal Experimentation Committee guidelines. All of the experimental protocols involving live rats were reviewed and approved by the Animal Experimentation Committee of Chang Gung Memorial Hospital–Kaohsiung Medical Center. The rats were anesthetized with pentobarbital (dosage: 45 mg/kg of body weight) and then given Gd^{3+}-chelated Fe_3O_4@SiO_2 nanoparticles or Resovist (0.5 mg[Fe]/kg), dispersed in normal saline and injected *via* the tail vein with a 30G needle connected to a syringe with 50 cm polyethylene tubing. MR imaging was done on a 3T scanner (GE SIGNA EXCITE HD; GE Medical Systems, Milwaukee, WI) with a 100 mm diameter volume coil. Pilot images (repetition time msec/effective echo time ms, 660/11.6; number of acquisitions, four) and T_2-weighted (6350/86.1; number of acquisitions, four) fast spin–echo images were initially acquired to determine the optimal axial plane. For the BOLD MR images, in order to measure the R_2* values, a multiecho gradient echo sequence with 9 echoes was done on each rat, which yielded nine T_2*-weighted images with echo times (T_E) ranging from 2.8 to 29.6 ms in steps of 3.35 ms. Other scanning parameters included the following: repetition time (T_R) = 200 ms; flip angle =30°; bandwidth = 31.25 kHz; field of view = 12 × 12 cm; matrix = 192 × 192; and number of acquisitions = three. Eighteen axial slices with a thickness of 3 mm and no gap were acquired.

Data Analysis of BOLD MR Imaging. Using FuncTool on an Advantage workstation (GE Healthcare Biosciences, Piscataway, NJ), color R_2 and R_2* maps were generated and regions of interest (ROIs) were placed in the liver parenchyma (outside of the vascular structure of the liver graft) by a radiologist experienced with BOLD MR imaging. More specifically, two sections were obtained through the liver in the axial plane and up to three ROIs were placed per section in the liver parenchyma. A total of 6 ROIs per liver per rat were placed. Areas of obvious susceptibility to artifacts were avoided. R_2* values (1 s) were expressed as means ± standard deviations. Statistical analyses of liver parenchymal R_2* values were done using a two-sample *t* test with SPSS.

***In Vivo* Micro-MR Imaging.** Male BALB/c mice (6–8 weeks old) were provided by the National Taiwan University Laboratory Animal Center (Tainan, Taiwan). All mice received humane care in compliance with National Taiwan University's guidelines for maintenance and use of laboratory animals in research. All of the experimental protocols involving live mice were reviewed and approved by the Animal Experimentation Committee of National Taiwan University. Sequential MR images were acquired in a 7T MR imager (BioSpec 70/30 USR; Bruker) equipped with a high-performance transmitter–receiver volume coil (BGA6-S; Bruker) (inner diameter: 6 cm) with a maximal gradient strength of 200 mT m^{-1}. The mice were anesthetized using 2% isoflurane (Abbott Laboratories, Abbott Park, IL) mixed with 100% O_2 delivered using a veterinary anesthesia delivery system (ADS 1000; Engler Engineering, Hialeah, FL), and then given Gd^{3+}-chelated Fe_3O_4@SiO_2 nanoparticles (0.5 mg[Fe]/kg) dispersed in normal saline, and injected *via* the jugular vein using PE-8 polyethylene tubing. Gd^{3+}-chelated Fe_3O_4@SiO_2 nanoparticles yielded a signal contrast using a TuborRARE T2 pulse sequence (TR/TE/FA, 4000 ms/33 ms/180°; MTX, 256 × 192 × 17; FOV, 40 × 30 × 1 mm^3) and a NEX of 8.

Biodistribution of Nanocontrast Agents. BALB/C mice (male, 8–12 weeks old) were purchased from the Laboratory Animal Center of National Cheng Kung University and maintained in a pathogen-free facility. The mice were raised and cared for according to the guidelines set up by the National Science Council, Taiwan. The mouse experiments were approved by National Cheng Kung University's Animal Care and Use Committee. Mice were injected *via* the tail vein with 100 μL of 0.5 mg [Fe]/kg Gd^{3+}-chelated Fe_3O_4@SiO_2 nanoparticles and Resovist (n = 3). Three additional noninjected mice were included as controls. At 0.5, 2.5, 12, and 24 h postinjection, the mice were euthanized, and blood and four different organs (kidneys, spleen, liver, and lungs) were collected to quantify the iron content using ICP-AES.

Measuring Alanine Aminotransferase (ALT) and Cytokine Levels. After the mice had been given 100 μL of 0.5 mg [Fe]/kg Gd^{3+}-chelated Fe_3O_4@SiO_2 nanoparticles and Resovist, their blood was collected from the retro-orbital sinus at specified time points. The activities of serum AST and ALT were analyzed using an automatic biochemistry analyzer (Roche Hitachi 717; Hitachi Koki Co., Ltd., Tokyo, Japan). Serum TNF-α and IL-6 were analyzed using an ELISA kit following the manufacturer's protocol (R&D Systems Inc., Minneapolis, MN).

Histopathologic and Immunohistochemical Assessments. Mice were intravenously injected with 0.5 or 5 mg/kg nanoparticles for 24 h and underwent physical evaluations. Portions of liver, spleen, kidney, and lung tissue were fixed in 3.7% formaldehyde (Merck, Whitehouse Station, NJ) at room temperature and then embedded in paraffin blocks. Tissue sections 5 μm thick were stained with hematoxylin and eosin. The morphology of the tissue was observed under a microscope at 10× and 20× magnification. The deparaffinized tissue sections were also stained with monoclonal rat anti-F4/80 antibody (eBioscience, San Diego, CA) for Kupffer cells. For fluorescent imaging, tissues were embedded in OCT and kept frozen at −80 °C. The frozen tissues were sliced in 5 μm thick sections and mounted on glass slides. The tissue sections were also stained with monoclonal rat anti-F4/80 antibody. Kupffer cell density was determined by

averaging the number of F4/80$^+$ cells in three areas of random microscopic fields (at 200× magnification) in each section.

Tissue Iron Staining. Deparaffinized tissue sections were stained with a modified diaminobenzidine-enhanced Perls iron stain as previously described.[40] Before they were iron stained, the deparaffinized tissue sections were incubated for 30 min in 6 N HCl to dissolve Fe_3O_4. Tissue sections were then incubated for 30 min in 1% potassium ferrocyanide in 0.12 N HCl. Endogenous peroxidase activity was quenched for 20 min at room temperature in 3.7% H_2O_2 in phosphate buffered saline (PBS). The sections were rinsed in PBS and incubated for 6 min in 3, 3′-diaminobenzidine tetrahydrochloride (DAB) (DAB-Plus Substrate Kit; Zymed Laboratories Inc., San Francisco, CA). The nucleus was stained with hematoxylin.

Characterization. Electron micrographs were obtained using transmission electron microscopes (JEOL 3010 at 300 KV, Philips CM-200 at 200 KV, and Hitachi H-7500 TEM at 80 kV). The Raman spectra (exposure time: 60 s) were obtained using a Renishaw inVia Raman microscope (Renishaw plc, New Mills, Wotton-under-Edge, Gloucestershire, UK) equipped with a 632.8 nm air-cooled He−Ne laser as the exciting source. X-ray photoelectron spectra (XPS) (VG Scientific 210) were recorded using a Mg Kα source (12 kV and 10 mA). The binding energy scale was calibrated to 284.6 eV for the main (C ls) peak. The Fe and Gd ions were quantified using an inductively coupled plasma atomic emission spectrometer (ICP-AES, JY138 Spectroanalyzer; Horiba Jobin Yvon, Inc., Edison, NJ). IR spectra were measured using a KBr plate in a Fourier transformation infrared (FTIR) spectrometer (200E; Jasco International Co., Ltd., Tokyo, Japan). The zeta-potential of the Fe_3O_4@CTAB nanoparticles dispersed in an aqueous solution (pH = 6) was measured using a Zetasizer analyzer (Malvern Instruments Ltd., Malvern, Worcestershire, UK). The $M-H$ magnetization curves at 300 K were measured for Fe_3O_4@SiO_2 and Gd^{3+}-chelated Fe_3O_4@SiO_2 nanoparticles using a magnetometer (MPMS-7 SQUID; Quantum Design, Inc., San Diego, CA).

Crystal Cell Information. The powder X-ray diffraction patterns of as-prepared Fe_3O_4 nanoparticles were recorded at the BL01C2 beamline of the National Synchrotron Radiation Research Center (NSRRC) in Taiwan. The NSRRC storage ring was operated at 1.5 GeV with a typical current of 360 mA. The wavelength of the incident X-rays was 0.49594 Å (25.0 keV), delivered from the superconducting wavelength-shifting magnet and a Si(111) double-crystal monochromator. The diffraction pattern was recorded with a Mar345 imaging plate detector located approximately 300 mm from the sample and with a typical exposure duration of 2 min. The pixel size of the Mar345 was 100 μm. The one-dimensional powder diffraction profile was converted with the FIT2D program (http://www.esrf.eu/computing/scientific/FIT2D/) and cake-type integration. The diffraction angles were calibrated according to the Bragg positions of Ag-Benhenate and Si powder (NBS640b) standards. The crystal structure refinement with the Rietveld method was performed with the GSAS program (http://www.ncnr.nist.gov/xtal/software/gsas.html).

Acknowledgment. This work was supported by the National Science Council, Taiwan, under NSC 99-2627-M-006-008 and NSC99-2120-M-006-008. We thank Prof. Jyh-Horng Chen for valuable help with the 7T MRI system, and Ms. Kuei-Fen Liao for valuable assistance with SAXS measurements.

Supporting Information Available: HR-TEM, SQUID, XRD, FT-IR, XPS, pore size distribution, T_2-weighted images, T_1/T_2 relaxation rates of as-obtained Fe_3O_4 and Gd^{3+}-chelated Fe_3O_4@SiO_2 nanoparticles, and biodistribution. This material is available free of charge *via* the Internet at http://pubs.acs.org.

REFERENCES AND NOTES

1. Su, C. H.; Sheu, H. S.; Lin, C. Y.; Huang, C. C.; Lo, Y. W.; Pu, Y. C.; Weng, J. C.; Shieh, D.; Chen, J. H.; Yeh, C. S. Nanoshell Magnetic Resonance Imaging Contrast Agents. *J. Am. Chem. Soc.* **2007**, *129*, 2139–2146.
2. Huang, C. C.; Su, C. H.; Li, W. M.; Liu, T. Y.; Chen, J. H.; Yeh, C. S. Bifunctional Gd_2O_3/C Nanoshells for MR Imaging and NIR Therapeutic Applications. *Adv. Funct. Mater.* **2009**, *19*, 249–258.
3. Jang, J. T.; Nah, H.; Lee, J. H.; Moon, S. H.; Kim, M. G.; Cheon, J. Critical Enhancements of MRI Contrast and Hyperthermic Effects by Dopant-Controlled Magnetic Nanoparticles. *Angew. Chem., Int. Ed.* **2009**, *48*, 1234–1238.
4. Tromsdorf, U. I.; Bigall, N. C.; Kaul, M. G.; Bruns, O. T.; Nikolic, M. S.; Mollwitz, B.; Sperling, R. A.; Reimer, R.; Hohenberg, H.; Parak, W. J.; *et al.* Size and Surface Effects on the MRI Relaxivity of Manganese Ferrite Nanoparticle Contrast Agents. *Nano Lett.* **2007**, *7*, 2422–2427.
5. Tromsdorf, U. I.; Bruns, O. T.; Salmen, S. C.; Beisiegel, U.; Weller, H. A Highly Effective, Nontoxic T_1 MR Contrast Agent Based on Ultrasmall PEGylated Iron Oxide Nanoparticles. *Nano Lett.* **2009**, *9*, 4434–4440.
6. Duan, H.; Kuang, M.; Wang, X.; Wang, Y. A.; Mao, H.; Nie, S. Reexamining the Effects of Particle Size and Surface Chemistry on the Magnetic Properties of Iron Oxide Nanocrystals: New Insights into Spin Disorder and Proton Relaxivity. *J. Phys. Chem. C* **2008**, *112*, 8127–8131.
7. Hu, F.; MacRenaris, K. W.; Waters, E. A.; Liang, T.; Schultz-Sikma, E. A.; Eckermann, A. L.; Meade, T. J. Ultrasmall, Water-Soluble Magnetite Nanoparticles with High Relaxivity for Magnetic Resonance Imaging. *J. Phys. Chem. C* **2009**, *113*, 20855–20860.
8. Na, H. B.; Song, I. C.; Hyeon, T. Inorganic Nanoparticles for MRI Contrast Agents. *Adv. Mater.* **2009**, *21*, 2133–2148.
9. Powell, D. H.; Ni Dhubhghaill, O. M.; Pubanz, D.; Helm, L.; Lebedev, Y. S.; Schlaepfer, W.; Merbach, A. E. Structural and Dynamic Parameters Obtained from ^{17}O NMR, EPR, and NMRD Studies of Monomeric and Dimeric Gd^{3+} Complexes of Interest in Magnetic Resonance Imaging: An Integrated and Theoretically Self-Consistent Approach. *J. Am. Chem. Soc.* **1996**, *118*, 9333–9346.
10. Kim, J.; Kim, H. S.; Lee, N.; Kim, T.; Kim, H.; Yu, T.; Song, I. C.; Moon, W. K.; Hyeon, T. Multifunctional Uniform Nanoparticles Composed of a Magnetite Nanocrystal Core and a Mesoporous Silica Shell for Magnetic Resonance and Fluorescence Imaging and for Drug Delivery. *Angew. Chem., Int. Ed.* **2008**, *47*, 8438–8441.
11. Basly, B.; Felder-Flesch, D.; Perriat, P.; Billotey, C.; Taleb, J.; Pourroy, G.; Begin-Colin, S. Dendronized Iron Oxide Nanoparticles as Contrast Agents for MRI. *Chem. Commun.* **2010**, *10*, 985–987.
12. Tong, S.; Hou, S.; Zheng, Z.; Zhou, J.; Bao, G. Coating Optimization of Superparamagnetic Iron Oxide Nanoparticles for High T_2 Relaxivity. *Nano Lett.* **2010**, *10*, 4607–4613.
13. Bae, K. H.; Kim, Y. B.; Lee, Y.; Hwang, J. Y.; Park, H. W.; Park, T. G. Bioinspired Synthesis and Characterization of Gadolinium-Labeled Magnetite Nanoparticles for Dual Contrast T_1- and T_2-Weighted Magnetic Resonance Imaging. *Bioconjugate Chem.* **2010**, *21*, 505–512.
14. Kim, H. H.; Lee, C. H.; Lee, S. K. Superparamagnetic Gd- and Mn-Substituted Magnetite Fluids Applied as MRI Contrast Agents. *Bull. Korean Chem. Soc.* **2009**, *30*, 1305–1308.
15. Daou, T. J.; Pourroy, G.; Bégin-Colin, S.; Grenèche, J. M.; Ulhaq-Bouillet, C.; Legaré, P.; Bernhardt, P.; Leuvrey, C.; Rogez, G. Hydrothermal Synthesis of Monodisperse Magnetite Nanoparticles. *Chem. Mater.* **2006**, *18*, 4399–4404.
16. Vereda, F.; de Vicente, J.; del Puerto Morales, M.; Rull, F.; Hidalgo-Alvarez, R. Synthesis and Characterization of Single-Domain Monocrystalline Magnetite Particles by Oxidative Aging of $Fe(OH)_2$. *J. Phys. Chem. C* **2008**, *112*, 5843–5849.
17. Prozorov, R.; Prozorov, T.; Mallapragada, S. K.; Narasimhan, B.; Williams, T. J.; Bazylinski, D. A. Magnetic Irreversibility and the Verwey Transition in Nanocrystalline Bacterial Magnetite. *Phys. Rev. B* **2007**, *76*, 054406(1)–(9).
18. Yang, J. B.; Zhou, X. D.; Yelon, W. B.; James, W. J.; Cai, Q.; Gopalakrishnan, K. V.; Malik, S. K.; Sun, X. C.; Nikles, D. E. Magnetic and Structural Studies of the Verwey Transition in $Fe_{3-\delta}O_4$ Nanoparticles. *J. Appl. Phys.* **2004**, *95*, 7540–7542.

19. Shavel, A.; Liz-Marzán, L. M. Shape Control of Iron Oxide Nanoparticles. *Phys. Chem. Chem. Phys.* **2009**, *11*, 3762–3766.
20. Lin, H.-P.; Mou, C.-Y. Structural and Morphological Control of Cationic Surfactant-Templated Mesoporous Silica. *Acc. Chem. Res.* **2002**, *35*, 927–935.
21. Gorelikov, I.; Matsuura, N. Single-Step Coating of Mesoporous Silica on Cetyltrimethyl Ammonium Bromide-Capped Nanoparticles. *Nano Lett.* **2008**, *8*, 369–373.
22. Paula, A. J.; Stéfani, D.; Filho, A. G. S.; Kim, Y. A.; Endo, M.; Alves, O. L. Surface Chemistry in the Process of Coating Mesoporous SiO_2 onto Carbon Nanotubes Driven by the Formation of Si−O−C Bonds. *Chem.—Eur. J.* **2011**, *17*, 3228–3237.
23. Lin, H.-P.; Yang, L.-Y.; Mou, C.-Y.; Liu, S.-B.; Lee, H.-K. *New J. Chem.* **2000**, *24*, 253–255.
24. Kimura, T.; Saeki, S.; Sugahara, Y.; Kuroda, K. Organic Modification of FSM-Type Mesoporous Silicas Derived from Kanemite by Silylation. *Langmuir* **1999**, *15*, 2794–2798.
25. Liu, Y.-H.; Lin, H.-P.; Mou, C.-Y. Direct Method for Surface Silyl Functionalization of Mesoporous Silica. *Langmuir* **2004**, *20*, 3231–3239.
26. Hu, K.-W.; Hsu, K.-C.; Yeh, C.-S. pH-Dependent Biodegradable Silica Nanotubes Derived from $Gd(OH)_3$ Nanorods and Their Potential for Oral Drug Delivery and MR Imaging. *Biomaterials* **2010**, *31*, 6843–6848.
27. Tsai, C.-P.; Hung, Y.; Chou, Y.-H.; Huang, D.-M.; Hsiao, J.-K.; Chang, C.; Chen, Y.-C.; Mou, C.-Y. High-Contrast Paramagnetic Fluorescent Mesoporous Silica Nanorods as a Multifunctional Cell-Imaging Probe. *Small* **2008**, *4*, 186–191.
28. Lin, Y. S.; Hung, Y.; Su, J. K.; Lee, R.; Chang, C.; Lin, M. L.; Mou, C. Y. Gadolinium(III)-Incorporated Nanosized Mesoporous Silica as Potential Magnetic Resonance Imaging Contrast Agents. *J. Phys. Chem. B* **2004**, *108*, 15608–15611.
29. Taylor, K. M. L.; Kim, J. S.; Rieter, W. J.; An, H.; Lin, W.; Lin, W. Mesoporous Silica Nanospheres as Highly Efficient MRI Contrast Agents. *J. Am. Chem. Soc.* **2008**, *130*, 2154–2155.
30. Liao, L.; Wang, H.; Wang, X.; Zhao, P.; Wang, S.; Su, W.; Chang, J. Multifunctional Nanoparticles Composed of A Poly(DL-lactide-*co*-glycolide) Core and a Paramagnetic Liposome Shell for Simultaneous Magnetic Resonance Imaging and Targeted Therapeutics. *Adv. Funct. Mater.* **2011**, *21*, 1179–1186.
31. Jeng, U.; Su, C. H.; Su, C.-J.; Liao, K.-F.; Chuang, W.-T.; Lai, Y.-H.; Chang, J.-W.; Chen, Y.-J.; Huang, Y.-S.; Lee, M.-T.; *et al.* A Small/Wide-Angle X-ray Scattering Instrument for Structural Characterization of Air−Liquid Interfaces, Thin Films and Bulk Specimens. *J. Appl. Crystallogr.* **2010**, *43*, 110–121.
32. Sheu, H.-S.; Jeng, U.; Shih, W.-J.; Lai, Y.-H.; Su, C.-H.; Lai, C.-W.; Yang, M.-J.; Chen, Y.-C.; Chou, P.-T. Phase Separation Inside the CdTe−CdSe Type II Quantum Dots Revealed by Synchrotron X-ray Diffraction and Scattering. *J. Phys. Chem. C* **2008**, *112*, 9617–9622.
33. Botta, M. Second Coordination Sphere Water Molecules and Relaxivity of Gadolinium(III) Complexes: Implications for MRI Contrast Agents. *Eur. J. Inorg. Chem.* **2000**, *2000*, 399–407.
34. Gueron, M. Nuclear Relaxation in Macromolecules by Paramagnetic Ions: A Novel Mechanism. *J. Magn. Reson.* **1975**, *19*, 58–66.
35. Hyder, F.; Kida, I.; Behar, K. L.; Kennan, R. P.; Maciejewski, P. K.; Rothman, D. L. Quantitative Functional Imaging of the Brain: Towards Mapping Neuronal Activity by BOLD fMRI. *NMR Biomed.* **2001**, *14*, 413–431.
36. Wood, J. C.; Enriquez, C.; Ghugre, N.; Tyzka, J. M.; Carson, S.; Nelson, M. D.; Coates, T. D. MRI R2 and R2* Mapping Accurately Estimates Hepatic Iron Concentration in Transfusion-Dependent Thalassemia and Sickle Cell Disease Patients. *Blood* **2005**, *106*, 1460–1465.
37. Jain, T. K.; Reddy, M. K.; Morales, M. A.; Leslie-Pelecky, D. L.; Labhasetwar, V. Biodistribution, Clearance, and Biocompatibility of Iron Oxide Magnetic Nanoparticles in Rats. *Mol. Pharmaceutics* **2008**, *5*, 316–327.
38. Hardonk, M. J.; Dijkhuis, F. W.; Hulstaert, C. E.; Koudstaal, J. Heterogeneity of Rat Liver and Spleen Macrophages in Gadolinium Chloride-Induced Elimination and Repopulation. *J. Leukocyte Biol.* **1992**, *52*, 296–302.
39. Yeh, C.-S.; Huang, C.-C. Iron Oxide Nanoparticles and the Production Method Thereof. ROC Patent 98135501, submitted.
40. Huang, F. W.; Pinkus, J. L.; Pinkus, G. S.; Fleming, M. D.; Andrews, N. C. A Mouse Model of Juvenile Hemochromatosis. *J. Clin. Invest.* **2005**, *115*, 2187–2191.